Letter

Tuning corner states in proximitized second-order topological insulators with bulk-boundary obstruction

Yang Xue,[1,*] Tong Zhou,[2,3] Wei Xu,[1] Bao Zhao,[4,5] Igor Žutić,[3] and Zhongqin Yang[4,6]

[1]*Department of Physics, East China University of Science and Technology, Shanghai 200237, China*
[2]*Eastern Institute for Advanced Study, Eastern Institute of Technology, Ningbo, Zhejiang 315200, China*
[3]*Department of Physics, University at Buffalo, State University of New York, Buffalo, New York 14260, USA*
[4]*State Key Laboratory of Surface Physics and Key Laboratory of Computational Physical Sciences (MOE) and Department of Physics, Fudan University, Shanghai 200433, China*
[5]*Shandong Key Laboratory of Optical Communication Science and Technology, School of Physics Science and Information Technology, Liaocheng University, Liaocheng 252059, China*
[6]*Shanghai Qi Zhi Institute, Shanghai 200030, China*

(Received 12 December 2022; revised 12 October 2023; accepted 13 October 2023; published 24 October 2023; corrected 5 March 2024)

Second-order topological insulators (SOTIs) support topological states beyond the usual bulk-boundary correspondence and provide important connections between quantum chemistry and topology. A hallmark of the two-dimensional (2D) SOTIs is the emergence of corner states, which usually arise from the topologically nontrivial obstructed states in the bulk. In contrast, we reveal a very different scenario where even trivial obstructed bulk states can induce corner states due to their open boundaries. Remarkably, we show that these two types of corner states can coexist in a single system and predict, from first-principles calculations, that the monolayer C_2N is a promising candidate for their observation. To overcome the limitation in manipulating corner states, we demonstrate it can be accomplished using a magnetic exchange field, where the corner states can be fully spin polarized and moved into the bulk states. Focusing on the example of the C_2N/CrI_3 van der Waals heterostructure, we put forth a class of proximitized materials which enable the versatile control of corner states through strain-controlled magnetic proximity effects. Our work reveals another type of topological state, and provides a universal proposal for topological corner state modulations and applications.

DOI: 10.1103/PhysRevB.108.L161110

Introduction. Higher-order topological insulators are a new class of topological crystalline phase characterized by a generalized bulk-boundary correspondence [1–4]. Unlike conventional topological insulators [5–13], their dimensional difference between the nontrivial boundary state and the bulk state is greater than 1. For example, a two-dimensional (2D) second-order topological insulator (SOTI) has 1D gapped edge states and 0D in-gap corner states (CSs) [14–20]. With the guidance of topological quantum chemistry [21] and related theories [22–26], 2D SOTIs are usually sought in unconventional materials [27] with bulk band representations (BRs) that can be decomposed into elementary BRs (eBRs), i.e., generators of BRs, but not atomic-orbital-induced BRs (aBRs), which correspond to trivial insulators. This absence of the aBR decomposition is known as the obstructed atomic limit (OAL), i.e., bulk obstruction [21,28–30]. The topologically nontrivial bulk obstruction is considered to be a key signature of SOTIs, where the eBR centers are displaced from the underlying atomic ions and thus generate electric multiple moments, inducing fractionally charged CSs [1,31,32].

However, even with a trivial bulk obstruction, we identify a scenario to realize CSs originating from the open boundary. Remarkably, we find that these two different types of CSs (from both nontrivial and trivial bulk obstructions) can coexist in SOTIs with bulk-boundary obstruction and can be realized in realistic materials, supported by our first-principles calculations. Unlike the well-studied manipulation of skyrmions or Majorana zero modes [33,34], the control of CSs as another class of topological defects is largely unexplored. Together with the experimental challenges of realizing SOTIs in real electronic materials, this lack of CS control limits their potential applications.

To overcome these challenges, we predict from symmetry analysis and first-principles calculations that C_2N, a synthesized monolayer (ML) [35,36], is the bulk-boundary obstructed SOTI. We further show a versatile CS control by a magnetic exchange field. This principle is verified in the van der Waals (vdW) heterostructure C_2N/CrI_3, where CrI_3 is a well-studied 2D magnet [37,38]. The CSs are tunable by using a vertical compressive strain which changes the proximity-induced exchange splitting. In addition to identifying a different SOTI and suggesting the 2D SOTI/2D magnet as a promising platform for CS control, our work extends the opportunities for proximitized materials [39,40] to implement higher-order topological insulators and superconductors [3,4].

Bulk-boundary obstruction. We study the bulk-boundary obstruction effect in a nearest-neighbor honeycomb lattice model with three p orbitals, where p_z orbitals are decoupled from (p_x, p_y) orbitals due to the planar lattice, as illustrated in

*xuey@ecust.edu.cn

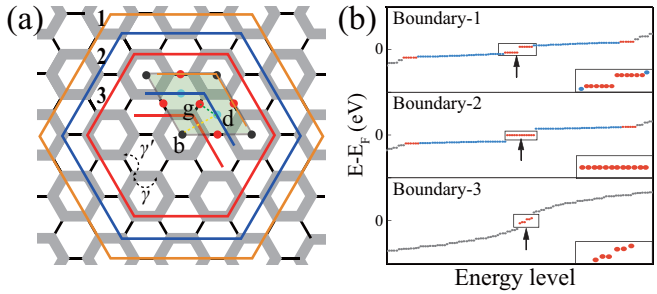

FIG. 1. (a) A Kekulé-honeycomb lattice: Thick (thin) bonds show intracellular, γ (intercellular, γ') hopping. Flake boundaries are labeled with different colors and numbers (1, 2, and 3). The corner regions of such boundaries and maximal Wyckoff positions ($1b$, $2d$, $3g$) indicated by the colorful dots are also given in a unit cell (green rhombus), where the yellow and green dashed lines denote equivalent paths for the Wannier centers of $h_{p_{xy}}$. (b) Energy spectra for (a) with various boundaries, where the numbers of the boundaries correspond to those in (a). The red, blue, and gray dots represent corner, edge, and bulk states, respectively. The black arrow denotes the Fermi levels by the electron counting, E_F. Inset: Enlarged CSs near E_F.

Fig. 1(a). The resulting total Hamiltonian H takes the form of $H = h_{p_z} \oplus h_{p_{x,y}}$, where h_{p_z} and $h_{p_{x,y}}$ denote the hopping terms in the p_z and (p_x, p_y) orbital subspaces, respectively. Further details regarding the model can be found in our Supplemental Material (SM) [41]. Previous work has shown that applying Kekulé modulation in the h_{p_z} [$\gamma < \gamma'$ in Fig. 1(a)] can lead to a bulk-obstructed SOTI with emergent CSs [18,42–45], as confirmed in our calculations [41]. However, it is unclear how the combined effect of the h_{p_z} and $h_{p_{x,y}}$ contributes to the topology and CSs of the H. To address these questions, we first investigate the topology of $h_{p_{x,y}}$ and subsequently explore the superposition effect of h_{p_z} and $h_{p_{x,y}}$.

To characterize the topology of the half-filling $h_{p_{x,y}}$, we calculate its symmetry indicators and related corner charges as

$$\chi^{(6)} = \left([M_1^{(2)}], [K_1^{(3)}]\right),$$
$$Q^{(6)}_{\text{corner}} = \frac{e}{4}[M_1^{(2)}] + \frac{e}{6}[K_1^{(3)}] \bmod e, \tag{1}$$

where the superscript 6 of $\chi^{(6)}$ and $Q^{(6)}_{\text{corner}}$ labels the C_6 symmetry of our model and the invariant $[\Pi_p^{(n)}]$, $\Pi = K$ or M, indicates the difference in the number of eigenvalues ($e^{2\pi i(p-1)/n}$) of C_n operation at Π and Γ in the occupied bands manifold [32]. The calculated irreducible representations (irreps) for the occupied bands of $h_{p_{x,y}}$ at several high-symmetry k points (HSKPs) are shown in Table I, which give a symmetry indicator $\chi^{(6)}_{h_{p_{x,y}}} = (0, 0)$, indicating the half-filling $h_{p_{x,y}}$ is topologically trivial and therefore no in-gap CSs are expected. However, the in-gap CSs are surprisingly found in the hexagonal flakes of the $h_{p_{x,y}}$ with boundaries 1 and 2 [Fig. 1(a)] [41], which contradicts the prediction of the symmetry indicator. We uncover the unanticipated CSs resulting from the boundary obstruction as follows.

As shown in Tables I and S1 [41], the occupied parts of $h_{p_{x,y}}$ cannot be decomposed as a sum of aBRs, but can be decomposed as a sum of eBRs induced from Wyckoff positions $1b$, $2d$, or $3g$, respectively. The site symmetry groups of Wyckoff positions $1b$, $2d$, and $3g$ are D_{6h}, D_{3h}, and D_{2h}, respectively. The high-symmetry lines ($1b \leftrightarrow 2d$) and ($2d \leftrightarrow 3g$) have site symmetry groups C_{2v} and C_s, respectively. Due to the relations

$$\begin{aligned}
&C_{2v} \subset (D_{6h} \cap D_{3h}),\\
&(A_1 \oplus 2B_1) \uparrow D_{3h} = E' \oplus A_2',\\
&(A_1 \oplus 2B_1) \uparrow D_{6h} = E_{2g} \oplus E_{1u} \oplus B_{2u} \oplus A_{2g},\\
&C_s \subset (D_{3h} \cap D_{2h}),\\
&A' \uparrow D_{2h} = B_{1g} \oplus B_{3u},\\
&A' \uparrow D_{3h} = E' \oplus A_2',
\end{aligned} \tag{2}$$

where the A_1 (B_1) and A' are the irreps of the C_{2v} and C_s, respectively, the three eBR decompositions for the occupied bands of the $h_{p_{x,y}}$ in Table I are equivalent [21,28]. In other words, the occupied bulk bands of $h_{p_{x,y}}$ are in trivial OAL, and their Wannier centers can adiabatically move between the $3g$, $2d$, and $1b$ sites through the lines ($1b \leftrightarrow 2d$) and ($2d \leftrightarrow 3g$) in periodic boundary conditions. These lines are depicted as the yellow and green dashed lines in Fig. 1(a). However, the equivalence between the Wannier states at these three Wyckoff positions will be broken by any open boundary termination that possesses these Wannier sites, as electron filling of these sites on the edge is half of its filling in the bulk (since such a site is shared by two unit cells). This results in an obstruction of these Wannier states in the open boundary conditions, referred to as a boundary (edge) obstruction [46], which gives rise to the CSs. As shown in Fig. 1(a), only terminations 1 and 2 allow some sites of the three Wyckoff positions to appear on the edges. The CSs of $h_{p_{x,y}}$ can only be obtained in nanoflakes with terminations 1 and 2 [41].

Next, we demonstrate the bulk-boundary obstruction with $H = h_{p_z} \oplus h_{p_{x,y}}$, whose energy bands are superpositions of the bands of h_{p_z} and $h_{p_{x,y}}$ [41]. The topological invariants and observables of H can be accessed from those of h_{p_z} and $h_{p_{x,y}}$ [32]. At half filling, the symmetry indicator of h_{p_z} is $\chi^{(6)}_{h_{p_z}} = (2, 0)$ [18] and of H is $\chi^{(6)}_H = \chi^{(6)}_{h_{p_{x,y}}} + \chi^{(6)}_{h_{p_z}} = (2, 0)$, the same as $\chi^{(6)}_{h_{p_z}}$. This implies that the in-gap CSs of H are the same as those of h_{p_z} and can only be obtained with termination 3 [41]. By calculating the hexagonal flakes of the H with terminations shown in Fig. 1(b), the in-gap CSs appear in all cases. By comparing Fig. 1(b) and Fig. S2 [41], we see that the appearance of the CSs of H in the flakes with terminations 1 and 2 is due to the boundary obstruction of $h_{p_{x,y}}$, while in

TABLE I. Irreps for the occupied bands of the $h_{p_{x,y}}$. The number in front of each irrep denotes its repeat times. The last row gives the three equivalent eBR decompositions of the occupied bands.

	Γ	M	K
Bands	$\Gamma_6^- \oplus \Gamma_5^+ \oplus \Gamma_3^- \oplus \Gamma_2^+$	$M_4^- \oplus 2M_3^- \oplus M_1^+ \oplus 2M_2^+$	$K_1 \oplus K_4 \oplus 2K_5$
Decomposition 1		$(B_{1g} \oplus B_{3u})@3g$	
Decomposition 2		$2(E' \oplus A_2')@2d$	
Decomposition 3		$(E_{2g} \oplus E_{1u} \oplus B_{2u} \oplus A_{2g})@1b$	

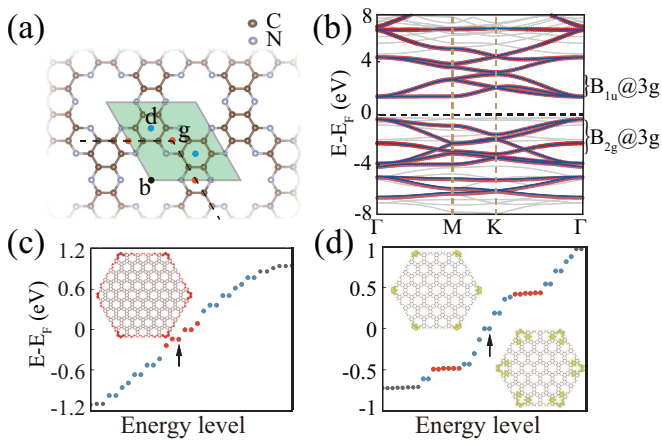

FIG. 2. (a) C_2N with maximal Wyckoff positions ($1b$, $2d$, $3g$) in the unit cell (green rhombus). Black-dashed lines: The flake boundaries for the CS calculations. (b) Orbital-resolved bands of C_2N with essential eBRs. Red dots: p_z orbitals; blue curves: fitted π bands using the Wannier method. (c) Calculated energy spectra for the π bands of C_2N hexagonal flakes with Wannier functions. Red, blue, and gray dots represent corner, edge, and bulk states. (d) Same as (c) but for C_2N using first-principles calculations. Charge distributions of the unoccupied (occupied) CSs are shown upper left (lower right).

the flake with termination 3 it is due to the nontrivial bulk topology of the h_{p_z} subspace.

Bulk-boundary obstructed SOTI in C_2N. We find the experimentally fabricated ML C_2N (for brevity C_2N) to be an ideal 2D SOTI with bulk-boundary combined obstruction. The C_2N is a semiconductor with a hexagonal planar structure [35,47,48], as shown in Fig. 2(a). Its has a $p6/mmm$ space group (No. 191) symmetry and consists of 12 C and six N atoms at Wyckoff positions $12q$ and $6k$. The C_2N has a combination of π bands (p_z) and σ bands (sp^2), due to the decoupling of its p_z orbitals from its sp^2 (s, p_x, p_y) orbitals. Since the spin-orbit coupling (SOC) in C_2N is small [41], it can be effectively neglected, allowing the material to be treated as spinless in this section.

The orbital-resolved energy bands [Fig. 2(b)] show half-filled π bands of C_2N. The calculated irreps for these π bands at several HSKPs are displayed in Table S2 [41]. The BRs of these π bands can be decomposed into an aBR $A''@12q$ corresponding C p_z orbitals, along with two essential eBRs $B_{2g}@3g$ and $B_{1u}@3g$, both located at empty sites $3g$ [represented by red dots in Fig. 2(a)]. These two essential eBRs correspond to the three highest valence bands and the three lowest conduction bands, respectively, shown in Fig. 2(b). The irreps of these essential eBRs are consistent with those of the 2D Kekulé distorted hexagonal model [18], suggesting that it can explain the low-energy physics and topological properties of the π bands. The occupied essential eBRs of the π bands, $B_{2g}@3g$, have a nonzero real-space invariant (RSI) $\delta_1@3g = -m(A_g) + m(A_u) - m(B_{1g}) + m(B_{1u}) - m(B_{3g}) + m(B_{3u}) - m(B_{2g}) + m(B_{2u}) = -1$ [49], which is the same as the one calculated with all the occupied C_2N bands and demonstrates the mismatch between the average electronic centers (Wyckoff sites $3g$) and the atomic positions (Wyckoff sites $6k$ and $12q$).

To verify the nontrivial topological properties of C_2N, we further calculated its symmetry indicators and topological CSs. The symmetry indicators from all the occupied C_2N bands are determined to be $\chi^{(6)} = (2, 0)$, which confirms that C_2N is in the OAL. Symmetry indicators calculated using only the occupied π bands of C_2N are the same as those calculated using all occupied bands, indicating that its nontrivial topological properties are determined by its π bands, in agreement with the above analysis.

The $\chi^{(6)} = (2, 0)$ topological invariant of C_2N suggests that the corner charge of the layer will be fractionalized with a value of $e/2$ in the spinless case and e in the spinful case for each $\pi/3$ sector. A half-filled 18-band tight-binding (TB) model based on Wannier functions, whose centers are located on the C and N atoms, shows good agreement with the π bands of C_2N [Fig. 2(b)]. The TB model of the hexagonal flake displayed six CSs at zero energy [Fig. 2(c)], in line with the symmetry indicators. A slight energy splitting of the in-gap CSs can be ascribed to the finite-size effect of the flake. However, when the same flake was calculated from first principles, there is a slight difference. The two groups of approximately sixfold degenerate states appear in the energy gap and the average corner charge was e, instead of $e/2$ for the spinless case, as shown in Fig. 2(d). This discrepancy can be understood by analyzing the remaining occupied σ bands.

As shown in Table S3 [41], the irreps of the occupied σ bands have trivial symmetry indicators [$\chi^{(6)} = (0, 0)$] and zero RSIs. The decompositions of the irreps means that the Wannier centers of sp^2 orbitals can be adiabatically moved between the $3g$, $2d$, and $1b$ sites. As we discussed in previous section, the equivalence between these sites is broken by a boundary termination, leading to the formation of six new half-filling CSs. The total corner charge in each $\pi/3$ sector of the spinless C_2N flake is e, contributed by CSs from the π and σ bands, respectively. Thus, C_2N is a different bulk-boundary obstructed 2D SOTI, with its corner charge simultaneously derived from both the nontrivial obstructed subspace (π bands) and the trivial obstructed subspace (σ bands) of its occupied bulk states.

Tailoring CSs in 2D SOTI/2D magnet heterostructures. We next show that the magnetic exchange field M can effectively manipulate the CSs of the 2D SOTIs based on a spinful Kekulé model [42],

$$H = \sum_{\langle ij\rangle,s} t_{ij} c_{is}^{\dagger} c_{js} + M \sum_{i} c_i^{\dagger} \sigma_z c_i, \tag{3}$$

where $\langle ij\rangle$ are the nearest neighbors on the honeycomb lattice, the transfer integral t_{ij} is γ (γ') on bold (thin) bonds in Fig. 1(a), and the $s = \{\uparrow / \downarrow\}$ represents the spin up/down, respectively. The second term represents an out-of-plane magnetic exchange field with its strength, M, and Pauli matrix, σ_z.

A finite M splits the spin-degenerate energy levels into spin-polarized energy levels, both for bulk and corner (edge) states. As shown in Fig. 3(a), the spin-degenerate in-gap CSs at the Fermi level, E_F, are divided into two groups [middle panel in Fig. 3(a)], with one occupied and one unoccupied, due to $M \neq 0$ and the requirement of charge conservation. Both sets of CSs are fully spin polarized, allowing for manipulation of the spin-degenerate CSs into energetically

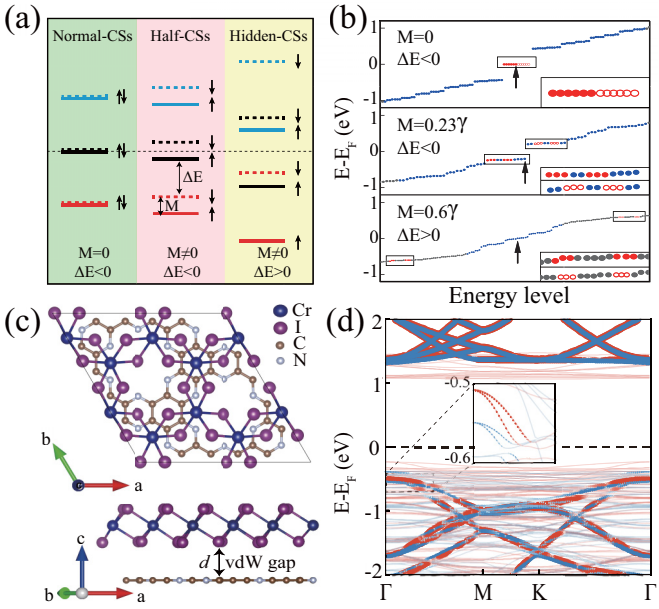

FIG. 3. (a) A schematic for the energy-level evolution of Eq. (2) tuned by a magnetic exchange field M, showing three types of CSs with specific M and ΔE, where ΔE represents the energy difference between the VBM and lowest CSs. The solid (dashed) lines: spin-up (spin-down) states. The colors of the lines, black (red), indicate the bulk (corner) states. (b) M-dependent energy spectra for Eq. (2) with $\gamma'/\gamma = 1.25$, where the colored dots and the black arrow have the same meaning as in Fig. 2. Solid (open) circles: spin-up (spin-down) CSs. (c) A vdW heterostructure C_2N/CrI_3. (d) Bands for (c), where the red (blue) dots indicate the spin-up (spin-down) p_z orbitals in C_2N.

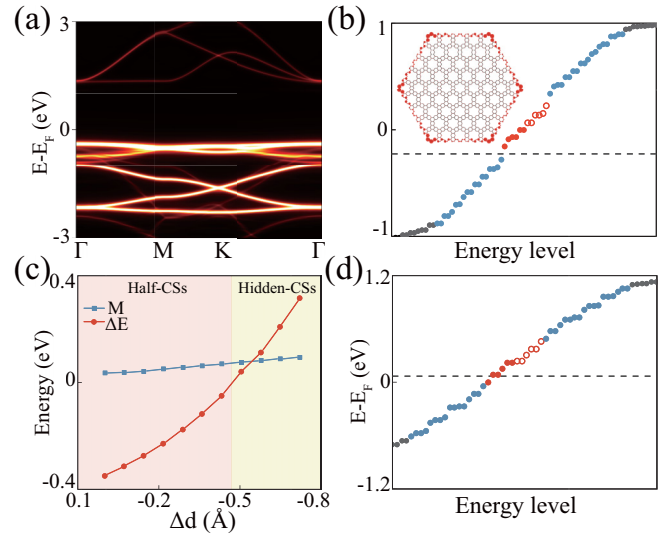

FIG. 4. (a) Unfolded bands of C_2N in the C_2N/CrI_3 heterostructure. (b) Same as Fig. 2(c) but for C_2N/CrI_3 heterostructures, where the dashed line indicates its VBM. The solid (open) circles indicate the spin-up (spin-down) CSs. (c) The evolution of M and ΔE tuned by the reduction of the vdW gap, Δd. (d) Same as (b) but with $\Delta d = -0.48$ Å.

distinguishable half CSs by applying M. As M increases, the CSs move further away from the E_F until they finally become hidden in the bulk states [right panel in Fig. 3(a)]. To simulate the M manipulation of CS, calculations were performed on open flakes of the magnetic Kekulé model. As shown in Fig. 3(b), the CSs (red) evolve consistently with the process described above, with half CSs appearing [middle panel in Fig. 3(b)].

To realize this CS control in SOTI, we propose its materials implementation in a C_2N/CrI_3 heterostructure [Fig. 3(c)], with structural details in the SM [41]. The p_z orbital-resolved spin-polarized bands of the heterostructure are plotted in Fig. 3(d), with an optimized equilibrium vdW gap, $d_0 = 3.61$ Å. For the calculated $\sqrt{3} \times \sqrt{3}$ supercell of C_2N, the bands were unfolded onto the k points in the Brillouin zone of the primitive cell of C_2N [Fig. 4(a)] by using the k-projection method [50]. The results show that C_2N was slightly magnetized by CrI_3.

We next focus on the lower-energy CSs of the C_2N/CrI_3 heterostructure, originating from the π bands of C_2N. The spinful TB model for the π bands of C_2N with M is used based on Wannier functions. As denoted in Fig. 3(d), M in the TB model can be estimated from the spin splitting of the low-energy π bands, which is about 35.7 meV and slightly larger than that in the graphene/CrI_3 [39]. The valence band maximum (VBM) of the C_2N/CrI_3 heterostructure can be measured from the valence π bands. As shown in Fig. 4(b), the results of the hexagonal flake of the spinful π-band model with $M \neq 0$ reveal a tiny spin splitting between the two groups of CSs with different spins. The VBM of C_2N/CrI_3 heterostructure, as depicted by the black dashed line in Fig. 4(b), is located below the lowest CSs. This result suggests the presence of the in-gap half CSs, such that the C_2N/CrI_3 heterostructure is in the phase depicted in the middle (pink) panel in Fig. 3(a).

Reducing the vdW gap can effectively enhance M and alter the energy difference between the bulk states and CSs, ΔE. Experimentally, this can be realized by applying external pressure with the goal to tune the pristine C_2N/CrI_3 heterostructure into a phase with hidden CSs [yellow panel in Fig. 3(a)]. Figure 4(c) shows the evolution of M and ΔE in the C_2N/CrI_3 heterostructure as a function of its reduced vdW gap, $\Delta d = d_0 - d$. When the vdW gap is reduced by approximately $\Delta d = -0.48$ Å, this yields $\Delta E > 0$ and implies that the lower group of CSs in the C_2N/CrI_3 heterostructure become hidden states under a compressive strain >0.48 Å. The energy levels of the hexagonal flake for the compressed C_2N/CrI_3 heterostructure with $\Delta d = -0.51$ Å are presented in Fig. 4(d), where the energy of the lower CSs is found to be below the VBM, consistent with the results shown in Fig. 4(c).

Our findings therefore reveal that the predicted bulk-boundary obstruction is another path towards 2D SOTIs, supported by symmetry analysis, tight-binding models, and first-principles calculations where we identify the C_2N monolayer as a suitable materials candidate. The presence of strain-tunable magnetic proximity effects, verified in C_2N/CrI_3 vdW heterostructures, offers an important prospect for a versatile control of the underlying CSs, which could be made fully spin polarized or hidden by being pushed into the bulk states. These findings suggest an exciting

opportunity to introduce superconducting proximity effects within our magnetic vdW heterostructures, potentially transforming SOTIs into second-order topological superconductors [51]. This implies that our CS manipulation method might be extended to control Majorana zero modes, enabling the exploration of their non-Abelian braiding or fusion processes [52–55].

Acknowledgments. We thank Dr. Zhongbo Yan for a very helpful discussion. This work was supported by National Natural Science Foundation of China under Grants No. 11904101 (Y.X.), No. 11604134 (B.Z.), No. 11874117 (Z.Y.), and No. 12174059 (Z.Y.), the Natural Science Foundation of Shanghai under Grant No. 21ZR1408200 (Z.Y.), and the U.S. DOE, Office of Science BES, Grant No. DE-SC0004890 (T.Z. and I.Ž.).

[1] W. A. Benalcazar, B. A. Bernevig, and T. L. Hughes, Quantized electric multipole insulators, Science **357**, 61 (2017).
[2] F. Schindler, A. M. Cook, M. G. Vergniory, Z. Wang, S. S. P. Parkin, B. A. Bernevig, and T. Neupert, Higher-order topological insulators, Sci. Adv. **4**, eaat0346 (2018).
[3] B. Xie, H.-X. Wang, X. Zhang, P. Zhan, J.-H. Jiang, M. Lu, and Y. Chen, Higher-order band topology, Nat. Rev. Phys. **3**, 520 (2021).
[4] B. J. Wieder, B. Bradlyn, J. Cano, Z. Wang, M. G. Vergniory, L. Elcoro, A. A. Soluyanov, C. Felser, T. Neupert, N. Regnault, and B. A. Bernevig, Topological materials discovery from crystal symmetry, Nat. Rev. Mater. **7**, 196 (2022).
[5] C. L. Kane and E. J. Mele, Z_2 topological order and the quantum spin Hall effect, Phys. Rev. Lett. **95**, 146802 (2005).
[6] L. Fu, C. L. Kane, and E. J. Mele, Topological insulators in three dimensions, Phys. Rev. Lett. **98**, 106803 (2007).
[7] B. A. Bernevig, T. L. Hughes, and S.-C. Zhang, Quantum spin Hall effect and topological phase transition in HgTe quantum wells, Science **314**, 1757 (2006).
[8] M. Z. Hasan and C. L. Kane, *Colloquium*: Topological insulators, Rev. Mod. Phys. **82**, 3045 (2010).
[9] X.-L. Qi and S.-C. Zhang, Topological insulators and superconductors, Rev. Mod. Phys. **83**, 1057 (2011).
[10] R. Yu, W. Zhang, H.-J. Zhang, S.-C. Zhang, X. Dai, and Z. Fang, Quantized anomalous Hall effect in magnetic topological insulators, Science **329**, 61 (2010).
[11] C.-Z. Chang, J. Zhang, X. Feng, J. Shen, Z. Zhang, M. Guo, K. Li, Y. Ou, P. Wei, L.-L. Wang, Z.-Q. Ji, Y. Feng, S. Ji, X. Chen, J. Jia, X. Dai, Z. Fang, S.-C. Zhang, K. He, Y. Wang *et al.*, Experimental observation of the quantum anomalous Hall effect in a magnetic topological insulator, Science **340**, 167 (2013).
[12] F. Reis, G. Li, L. Dudy, M. Bauernfeind, S. Glass, W. Hanke, R. Thomale, J. Schäfer, and R. Claessen, Bismuthene on a SiC substrate: A candidate for a high-temperature quantum spin Hall material, Science **357**, 287 (2017).
[13] D. Culcer, A. Cem Keser, Y. Li, and G. Tkachov, Transport in two-dimensional topological materials: Recent developments in experiment and theory, 2D Mater. **7**, 022007 (2020).
[14] M. Ezawa, Higher-order topological insulators and semimetals on the breathing kagome and pyrochlore lattices, Phys. Rev. Lett. **120**, 026801 (2018).
[15] X.-L. Sheng, C. Chen, H. Liu, Z. Chen, Z.-M. Yu, Y. X. Zhao, and S. A. Yang, Two-dimensional second-order topological insulator in graphdiyne, Phys. Rev. Lett. **123**, 256402 (2019).
[16] B. Liu, G. Zhao, Z. Liu, and Z. F. Wang, Two-Dimensional quadrupole topological insulator in γ-graphyne, Nano Lett. **19**, 6492 (2019).
[17] S. K. Radha and W. R. L. Lambrecht, Buckled honeycomb antimony: Higher order topological insulator and its relation to the Kekulé lattice, Phys. Rev. B **102**, 115104 (2020).
[18] Y. Xue, H. Huan, B. Zhao, Y. Luo, Z. Zhang, and Z. Yang, Higher-order topological insulators in two-dimensional Dirac materials, Phys. Rev. Res. **3**, L042044 (2021).
[19] J. Zeng, H. Liu, H. Jiang, Q.-F. Sun, and X. C. Xie, Multiorbital model reveals a second-order topological insulator in 1H transition metal dichalcogenides, Phys. Rev. B **104**, L161108 (2021).
[20] S. Qian, C.-C. Liu, and Y. Yao, Second-order topological insulator state in hexagonal lattices and its abundant material candidates, Phys. Rev. B **104**, 245427 (2021).
[21] B. Bradlyn, L. Elcoro, J. Cano, M. G. Vergniory, Z. Wang, C. Felser, M. I. Aroyo, and B. A. Bernevig, Topological quantum chemistry, Nature (London) **547**, 298 (2017).
[22] H. C. Po, A. Vishwanath, and H. Watanabe, Symmetry-based indicators of band topology in the 230 space groups, Nat. Commun. **8**, 50 (2017).
[23] Z. Song, T. Zhang, Z. Fang, and C. Fang, Quantitative mappings between symmetry and topology in solids, Nat. Commun. **9**, 3530 (2018).
[24] T. Zhang, Y. Jiang, Z. Song, H. Huang, Y. He, Z. Fang, H. Weng, and C. Fang, Catalogue of topological electronic materials, Nature (London) **566**, 475 (2019).
[25] F. Tang, H. C. Po, A. Vishwanath, and X. Wan, Comprehensive search for topological materials using symmetry indicators, Nature (London) **566**, 486 (2019).
[26] M. G. Vergniory, L. Elcoro, C. Felser, N. Regnault, B. A. Bernevig, and Z. Wang, A complete catalogue of high-quality topological materials, Nature (London) **566**, 480 (2019).
[27] J. Gao, Y. Qian, H. Jia, Z. Guo, Z. Fang, M. Liu, H. Weng, and Z. Wang, Unconventional materials: The mismatch between electronic charge centers and atomic positions, Sci. Bull. **67**, 598 (2022).
[28] J. Cano, B. Bradlyn, Z. Wang, L. Elcoro, M. G. Vergniory, C. Felser, M. I. Aroyo, and B. A. Bernevig, Building blocks of topological quantum chemistry: Elementary band representations, Phys. Rev. B **97**, 035139 (2018).
[29] B. Bradlyn, Z. Wang, J. Cano, and B. A. Bernevig, Disconnected elementary band representations, fragile topology, and Wilson loops as topological indices: An example on the triangular lattice, Phys. Rev. B **99**, 045140 (2019).
[30] Z. Song, Z. Fang, and C. Fang, $(d-2)$-dimensional edge states of rotation symmetry protected topological states, Phys. Rev. Lett. **119**, 246402 (2017).
[31] W. A. Benalcazar, B. A. Bernevig, and T. L. Hughes, Electric multipole moments, topological multipole moment pumping,

and chiral hinge states in crystalline insulators, Phys. Rev. B **96**, 245115 (2017).
[32] W. A. Benalcazar, T. Li, and T. L. Hughes, Quantization of fractional corner charge in C_n-symmetric higher-order topological crystalline insulators, Phys. Rev. B **99**, 245151 (2019).
[33] A. Fert, V. Cros, and J. Sampaio, Skyrmions on the track, Nat. Nanotechnol. **8**, 152 (2013).
[34] U. Güngördü and A. A. Kovalev, Majorana bound states with chiral magnetic textures, J. Appl. Phys. **132**, 041101 (2022).
[35] J. Mahmood, E. K. Lee, M. Jung, D. Shin, I.-Y. Jeon, S.-M. Jung, H.-J. Choi, J.-M. Seo, S.-Y. Bae, S.-D. Sohn, N. Park, J. H. Oh, H.-J. Shin, and J.-B. Baek, Nitrogenated holey two-dimensional structures, Nat. Commun. **6**, 6486 (2015).
[36] J. Xu, J. Mahmood, Y. Dou, S. Dou, F. Li, L. Dai, and J.-B. Baek, 2D frameworks of C_2N and C_3N as new anode materials for lithium-ion batteries, Adv. Mater. **29**, 1702007 (2017).
[37] B. Huang, G. Clark, E. Navarro-Moratalla, D. R. Klein, R. Cheng, K. L. Seyler, D. Zhong, E. Schmidgall, M. A. McGuire, D. H. Cobden, W. Yao, D. Xiao, P. Jarillo-Herrero, and X. Xu, Layer-dependent ferromagnetism in a van der Waals crystal down to the monolayer limit, Nature (London) **546**, 270 (2017).
[38] C. Gong and X. Zhang, Two-dimensional magnetic crystals and emergent heterostructure devices, Science **363**, eaav4450 (2019).
[39] J. Zhang, B. Zhao, T. Zhou, Y. Xue, C. Ma, and Z. Yang, Strong magnetization and Chern insulators in compressed graphene/CrI_3 van der Waals heterostructures, Phys. Rev. B **97**, 085401 (2018).
[40] I. Žutić, A. Matos-Abiague, B. Scharf, H. Dery, and K. Belashchenko, Proximitized materials, Mater. Today **22**, 85 (2019).
[41] See Supplemental Material at http://link.aps.org/supplemental/10.1103/PhysRevB.108.L161110 for an expanded discussion about the methods of first-principles calculations and the tight-binding model, structure details, symmetry analysis, and spin-orbit coupling influence, which includes Refs. [56–60].
[42] F. Liu, H.-Y. Deng, and K. Wakabayashi, Helical topological edge states in a quadrupole phase, Phys. Rev. Lett. **122**, 086804 (2019).
[43] F. Zangeneh-Nejad and R. Fleury, Nonlinear second-order topological insulators, Phys. Rev. Lett. **123**, 053902 (2019).
[44] T. Mizoguchi, H. Araki, and Y. Hatsugai, Higher-order topological phase in a honeycomb-lattice model with anti-Kekulé distortion, J. Phys. Soc. Jpn. **88**, 104703 (2019).
[45] E. Lee, A. Furusaki, and B.-J. Yang, Fractional charge bound to a vortex in two-dimensional topological crystalline insulators, Phys. Rev. B **101**, 241109(R) (2020).
[46] E. Khalaf, W. A. Benalcazar, T. L. Hughes, and R. Queiroz, Boundary-obstructed topological phases, Phys. Rev. Res. **3**, 013239 (2021).
[47] R. Zhang, B. Li, and J. Yang, Effects of stacking order, layer number and external electric field on electronic structures of few-layer C_2N-*h*2D, Nanoscale **7**, 14062 (2015).
[48] S. Gong, W. Wan, S. Guan, B. Tai, C. Liu, B. Fu, S. A. Yang, and Y. Yao, Tunable half-metallic magnetism in an atom-thin holey two-dimensional C_2N monolayer, J. Mater. Chem. C **5**, 8424 (2017).
[49] Z.-D. Song, L. Elcoro, and B. A. Bernevig, Twisted bulk-boundary correspondence of fragile topology, Science **367**, 794 (2020).
[50] M. Chen and M. Weinert, Layer k-projection and unfolding electronic bands at interfaces, Phys. Rev. B **98**, 245421 (2018).
[51] Z. Yan, Majorana corner and hinge modes in second-order topological insulator/superconductor heterostructures, Phys. Rev. B **100**, 205406 (2019).
[52] C. Nayak, S. H. Simon, A. Stern, M. Freedman, and S. Das Sarma, Non-Abelian anyons and topological quantum computation, Rev. Mod. Phys. **80**, 1083 (2008).
[53] D. Aasen, M. Hell, R. V. Mishmash, A. Higginbotham, J. Danon, M. Leijnse, T. S. Jespersen, J. A. Folk, C. M. Marcus, K. Flensberg, and J. Alicea, Milestones toward Majorana-based quantum computing, Phys. Rev. X **6**, 031016 (2016).
[54] T. Zhou, M. C. Dartiailh, W. Mayer, J. E. Han, A. Matos-Abiague, J. Shabani, and I. Žutić, Phase control of Majorana bound states in a topological X junction, Phys. Rev. Lett. **124**, 137001 (2020).
[55] T. Zhou, M. C. Dartiailh, K. Sardashti, J. E. Han, A. Matos-Abiague, J. Shabani, and I. Žutić, Fusion of Majorana bound states with mini-gate control in two-dimensional systems, Nat. Commun. **13**, 1738 (2022).
[56] G. Kresse and J. Furthmüller, Efficient iterative schemes for *ab initio* total-energy calculations using a plane-wave basis set, Phys. Rev. B **54**, 11169 (1996).
[57] J. P. Perdew, K. Burke, and M. Ernzerhof, Generalized gradient approximation made simple, Phys. Rev. Lett. **77**, 3865 (1996).
[58] A. A. Mostofi, J. R. Yates, Y.-S. Lee, I. Souza, D. Vanderbilt, and N. Marzari, Wannier90: A tool for obtaining maximally-localised Wannier functions, Comput. Phys. Commun. **178**, 685 (2008).
[59] Q. Wu, S. Zhang, H.-F. Song, M. Troyer, and A. A. Soluyanov, WannierTools: An open-source software package for novel topological materials, Comput. Phys. Commun. **224**, 405 (2018).
[60] J. Gao, Q. Wu, C. Persson, and Z. Wang, Irvsp: To obtain irreducible representations of electronic states in the VASP, Comput. Phys. Commun. **261**, 107760 (2021).

Correction: Support information in the Acknowledgment section was incomplete and has been fixed.